communications
physics

ARTICLE

https://doi.org/10.1038/s42005-021-00723-z OPEN

Resistivity saturation in Kondo insulators

Matthias Pickem[1], Emanuele Maggio[1] & Jan M. Tomczak[1]✉

Resistivities of heavy-fermion insulators typically saturate below a characteristic temperature T^*. For some, metallic surface states, potentially from a non-trivial bulk topology, are a likely source of residual conduction. Here, we establish an alternative mechanism: at low temperature, in addition to the charge gap, the scattering rate turns into a relevant energy scale, invalidating the semi-classical Boltzmann picture. Then, finite lifetimes of intrinsic carriers drive residual conduction, impose the existence of a crossover T^*, and control—now on par with the gap—the quantum regime emerging below it. Assisted by realistic many-body simulations, we showcase the mechanism for the Kondo insulator $Ce_3Bi_4Pt_3$, for which residual conduction is a bulk property, and elucidate how its saturation regime evolves under external pressure and varying disorder. Deriving a phenomenological formula for the quantum regime, we also unriddle the ill-understood bulk conductivity of SmB_6—demonstrating a wide applicability of our mechanism in correlated narrow-gap semiconductors.

---

[1] Institute of Solid State Physics, TU Wien, 1040 Vienna, Austria. ✉email: tomczak.jm@gmail.com

In Kondo insulators[1] the formation of bound-states between quasi-localized *f*-states and conduction electrons leads to the opening of a narrow hybridization gap at the Fermi level. When this hybridization is coherent, the resistivity exhibits an activation-type behavior. This semiconductor-like regime has as upper bound the Kondo lattice temperature, above which the local *f*-moments break free, inducing an insulator-to-metal crossover. This Kondo effect has been exhaustively studied over the last decades[2–4]. A more recent focus is the experimental observation of a lower bound to the semiconductor comportment, see Fig. 1 for the example of $Ce_3Bi_4Pt_3$[5–7]: below an inflection temperature T^* the resistivity levels off from exponential rise and enters a saturation regime—indicative of residual conduction. Possible explanations include exhaustion regimes (where extrinsic impurities pin the chemical potential), off-stoichiometry and impurity-band conduction[8,9], as well as, metallic surface states short-circuiting the gapped bulk. The latter can be an inevitable consequence of the non-trivial insulating bulk found in topological Kondo insulators[10].

Here, we develop an alternative mechanism in which residual conduction derives from finite lifetimes of intrinsic carriers of the (3D) bulk. We show that realistic many-body simulations, supplemented by a simple treatment for the disorder, capture the puzzling resistivity in the (non-topological) Kondo insulator $Ce_3Bi_4Pt_3$. We then distill essential ingredients from a reductionist model, establish a microscopic understanding, and provide a phenomenological form of the resistivity with which experiments can be readily analyzed. Our theory is applicable to other correlated narrow-gap semiconductors[4]: for mixed-valence SmB_6, we demonstrate that surface conduction coexists with our mechanism for a residual bulk conductivity—providing a definitive interpretation of recent experiments[11].

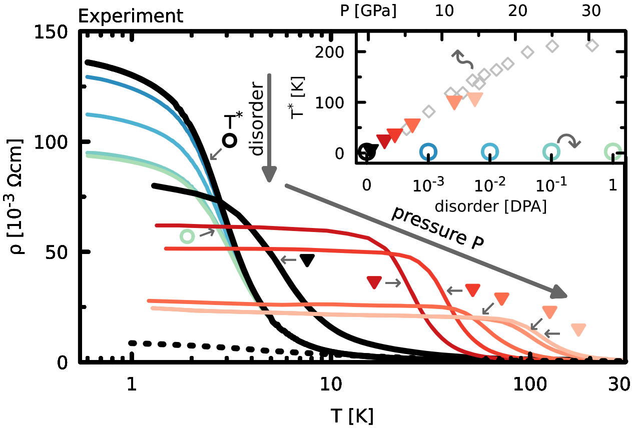

Fig. 1 Resistivity saturation in $Ce_3Bi_4Pt_3$. Below an inflection temperature T^* (indicated by small arrows), experimental resistivities $\rho(T)$[5-7] deviate from activation-like behavior ($T > T^*$) and enter a regime of resistivity saturation ($T < T^*$). Pressure and disorder affect the resistivity differently: under pressure (black and shades of red; from Cooley et al.[5]) the crossover temperature T^* (labeled with colored triangles and reported in the inset) grows significantly and the saturation value $\rho(T \to 0)$ decreases. Radiation-induced disorder (black and blue to green; from Wakeham et al.[6]) only suppresses $\rho(T \to 0)$, while T^* (labeled with colored circles and reported in the inset) remains constant. Also shown are results at ambient pressure from Katoh et al.[57] (dashed black line). Differences between black curves (solid and dashed) demonstrate a strong sample dependence. Inset: dependence of T^* on pressure (upper *x* axis; red-shaded triangles[5], gray diamonds from Campbell et al.[7]) and disorder (measured in displacements per atom (DPA); lower *x* axis; blue to green open circles[6]).

Results

The Kondo insulator $Ce_3Bi_4Pt_3$. Cubic intermetallic $Ce_3Bi_4Pt_3$ is a prototypical Kondo insulator[2,4,12]: spectroscopic[13,14] and susceptibility[12] measurements (also in high magnetic field[15,16]) are consistent with the Kondo scenario[17,18]. While a topological bulk state has been envisaged[19], experiments argue against surface-dominated transport[6]. Further constraints for a theory of resistivity saturation in $Ce_3Bi_4Pt_3$ come from, see Fig. 1: (i) pressure-dependent measurements that show a substantial increase in the crossover temperature T^*, accompanied by a decrease of the saturation value $\rho(T \to 0)$[5,7]; (ii) radiation-damaged samples in which residual conduction is successively suppressed, while T^* is unaffected[6]. In the following, we develop a microscopic theory encompassing these diverse experimental findings.

Many-body simulations vs. experiment. Using realistic many-body techniques, we simulate the bulk response of $Ce_3Bi_4Pt_3$ under pressure. In addition to renormalizations from electronic correlations—effective masses m^* and scattering rates $\Gamma(T)$—we mimic the effect of disorder[20] with an added scattering term Γ_{imp}. The resulting resistivities $\rho(T)$ are shown in Fig. 2 for varying (a) disorder and (b) pressure P. In all cases, we identify an inflection point T^* below which a saturation regime emerges: at ambient pressure, see Fig. 2a, a growing disorder (Γ_{imp}) causes T^* to only marginally increase. The saturation value $\rho(T \to 0)$, however, is notably suppressed as lifetimes shorten—congruent with experiments (Fig. 1). Applying pressure, see Fig. 2b, boosts T^* significantly, until it saturates between 20 and 30 GPa. The extracted T^*, reported in Fig. 3a, is in qualitative agreement with the experiment (Fig. 1 inset). Also, the saturation limit $\rho(T \to 0)$ depends strongly on pressure. In experiments, the trend in $\rho(T \to 0)$ varies, however, significantly between samples[5] and setups[5,7]. We, therefore, follow Campbell et al.[7] and reduce systematic errors by plotting in Fig. 3b the ratio $\rho_{\mathrm{base}}/\rho_{\mathrm{RT}}$ of the simulated resistivity at the lowest (base) temperature ($T = 1$ K) and at room temperature (RT: $T = 290$ K). In agreement with an experimental ratio at similar temperatures[7], we see an increase from $P = 0$ up to $P \sim 3$–5 GPa—the system becomes more insulating. For higher pressures, however, the ratio decreases again—mirroring the pressure-driven crossover to a bad insulator (cf. $\rho(T)$ in Fig. 2b). The simulations thus contain the necessary ingredients to account for the observed resistivity saturation in $Ce_3Bi_4Pt_3$, including its dependence on disorder and pressure. Next, we characterize the saturation regime in more detail and elucidate its origin using a microscopic model.

Microscopic theory. We consider a half-filled two-band ($n = 1, 2$) model with hopping t on the cubic lattice separated by a non-interacting gap Δ_0: $\epsilon^0_{\mathbf{k}n} = (-1)^n[2t\sum_{i=1,3}\cos(k_i) + (6t + \Delta_0/2)]$. We endow these dispersions with (i) a constant lifetime $\tau = \hbar/(2\Gamma_0)$ and (ii) a quasi-particle weight or mass enhancement $Z = m/m^* \le 1$. The latter renormalizes the dispersion, $\epsilon_{\mathbf{k}n} = Z\epsilon^0_{\mathbf{k}n}$, yields the interacting gap $\Delta = Z\Delta_0$, and dresses the scattering rate $\Gamma = Z\Gamma_0$. In the absence of particle-hole interactions, we can compute the linear-response conductivity of the model exactly (see "Method" section):

$$\sigma(T) = \frac{2\pi e^2\hbar}{V}\frac{Z^2}{4\pi^3}\frac{\beta}{\Gamma}\sum_{\mathbf{k}n} v^2_{\mathbf{k}n}\left(\mathrm{Re}\Psi'(z) - \frac{\beta\Gamma}{2\pi}\mathrm{Re}\Psi''(z)\right) \qquad (1)$$

with the inverse temperature $\beta = (k_B T)^{-1}$, the unit-cell volume V, (derivatives of) the digamma function $\Psi(z)$ evaluated at $z = \frac{1}{2} + \frac{\beta}{2\pi}(\Gamma + i\epsilon_{\mathbf{k}n})$, and the Fermi velocities $v_{\mathbf{k}n} = 1/\hbar\partial\epsilon^0_{\mathbf{k}n}/\partial\mathbf{k}$ in the Peierls approximation. The above formula is rich in physics:

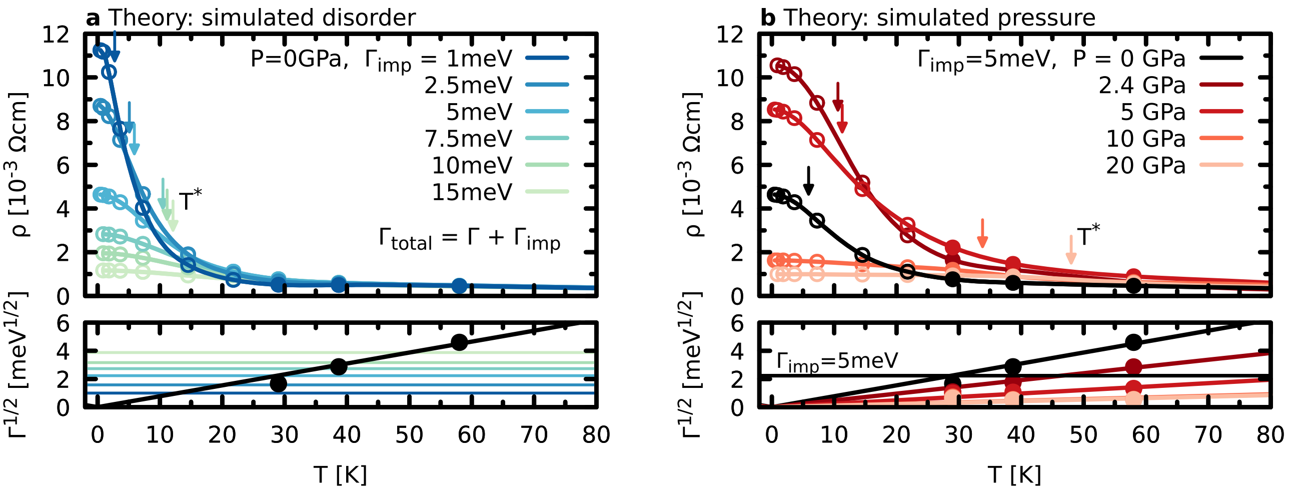

Fig. 2 Simulated resistivity of Ce$_3$Bi$_4$Pt$_3$. Shown are results for the resistivity $\rho(T)$ **a** at ambient pressure ($P = 0$) for varying impurity scattering Γ_{imp} (shades blue to green) and **b** at different pressures P (shades of red) for fixed impurity scattering $\Gamma_{\mathrm{imp}} = 5$ meV. Filled circles in $\rho(T)$ indicate simulation temperatures; results shown by open circles have been obtained by extrapolating the many-body scattering rate $\Gamma(T)$ with a quadratic fit. Vertical arrows indicate inflection points T^* in $\rho(T)$. The simulations mirror the experimental trends: T^* varies significantly with pressure, but depends only weakly on disorder. While transport simulations include the full self-energy $\Sigma(\omega)$, it is instructive to quantify electron-electron scattering: we display the square root of $\Gamma = -\langle \mathrm{Im}\Sigma(\omega = 0)\rangle_{J=5/2}$, the simulated many-body scattering rate at the Fermi level (averaged over Ce-4$fJ = 5/2$ components); black and red-shaded lines are linear fits to $\Gamma^{1/2}$ of simulated points, suggesting that for all pressures: $\Gamma = \gamma T^2$; γ decreases notably under compression, indicative of weakening correlation effects. Horizontal lines (shades of blue and green in **a**; dotted line in **b**) indicate the additional impurity-scattering rate Γ_{imp}. The total rate is the sum: $\Gamma_{\mathrm{total}} = \Gamma + \Gamma_{\mathrm{imp}}$.

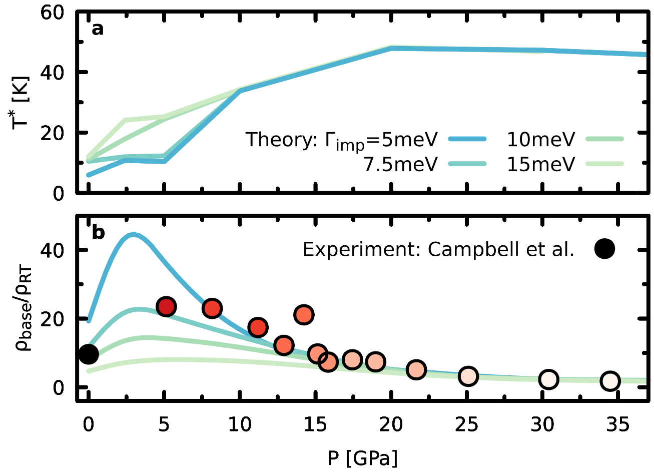

Fig. 3 Crossover temperature *T and resistivity ratio. a** Inflection temperatures T^* as a function of pressure for different impurity scatterings Γ_{imp} (lines shaded blue to green). At low pressures, T^* slightly depends on Γ_{imp}; above $P = 5$GPa, the onset of saturation is insensitive to the magnitude of impurity scattering. **b** Ratio of the resistivity at base temperature, ρ_{base}, and at room temperature (RT), ρ_{RT}, for different impurity scatterings Γ_{imp} (lines shaded blue to green), compared to experiment (circles; from ref. [7]). In the simulation (experiment[7]) the base and room temperatures were 1 and 290 K (2 and 300 K), respectively. The overall trend of the resistivity ratio with pressure is independent of the strength of impurity scattering. We find the best quantitative agreement with the experiment for $\Gamma_{\mathrm{imp}} \sim 7.5$meV.

in the coherent limit $\Gamma \to 0$, Eq. (1) simplifies to the well-known Boltzmann expression in the constant relaxation-time approximation[21]

$$\sigma(T) \overset{\Gamma\to 0}{=} \frac{e^2\hbar}{V}\frac{Z^2}{\Gamma}\sum_{\mathbf{k}n} v_{\mathbf{k}n}^2\left(-\partial f/\partial\omega\right)_{\omega=\epsilon_{\mathbf{k}n}}, \tag{2}$$

with the Fermi function f—albeit with a renormalization Z^2 commonly not included. In this semi-classical regime, the conductivity is simply proportional to the lifetime $\tau = \hbar/(2\Gamma)$. Then, for $k_BT \ll \Delta$, the resistivity has an activated form $\rho(T) \propto \exp(\Delta/(2k_BT))$ that diverges for $T \to 0$. In fact, here, Δ is the only relevant energy scale: as epitomized by Arrhenius-plot analyses, Δ single-handedly accounts for the archetypal $\rho(T)$ of semiconductors in the Boltzmann regime. There, resistance can be approximately described through electrons with sharply defined one-particle states (a band-structure $\epsilon_{\mathbf{k}n}$) that undergo collisions at a rate Γ, causing the charge current to decay on a timescale $\hbar/(2\Gamma)$. For sizable Γ, however, the broadening of the one-particle spectrum itself can no longer be neglected (Supplementary Note 1), spilling incoherent weight into the gap that contributes to conduction. This phenomenon is clearly beyond thermal activation across the gap. Still, Eq. (1) can be seen to retain an effective one-particle description (sharply defined dispersions), with many-body (lifetime) effects accounted for by a modified (Ψ-based) fermionic distribution function. To characterize the transport signatures of $\Gamma > 0$, we compute the resistivity $\rho(T) = 1/\sigma(T)$ according to Eq. (1), see Fig. 4. Akin to Ce$_3$Bi$_4$Pt$_3$, we see the emergence of a crossover temperature T^* below which $\rho(T)$ tends towards saturation. Since this phenomenon defies the semi-classical (Boltzmann) picture, we will label its domain the quantum regime. In conventional semiconductors, deviations from activated behavior typically occur when an extrinsic in-gap density pins the chemical potential. In the current scenario, impurity states influence conduction merely by limiting the lifetime of intrinsic carriers. Importantly, already minute scattering rates (mediated by impurities or other defects or couplings) lead to strong signatures at observable temperatures: in Fig. 4b, c, we indicate, respectively, the saturation limit $\rho(T \to 0)$ and the characteristic temperature T^* for the resistivities of the panel (a). In the relevant $\Gamma \ll \Delta$ regime, T^* changes more rapidly with Δ, whereas $\rho(T \to 0)$ is more sensitive to changes in Γ—as observed in experiments and simulations for Ce$_3$Bi$_4$Pt$_3$ (see above).

We can give more precise analytical insight: at low temperatures, the minimum (maximum) of conduction (valence) states

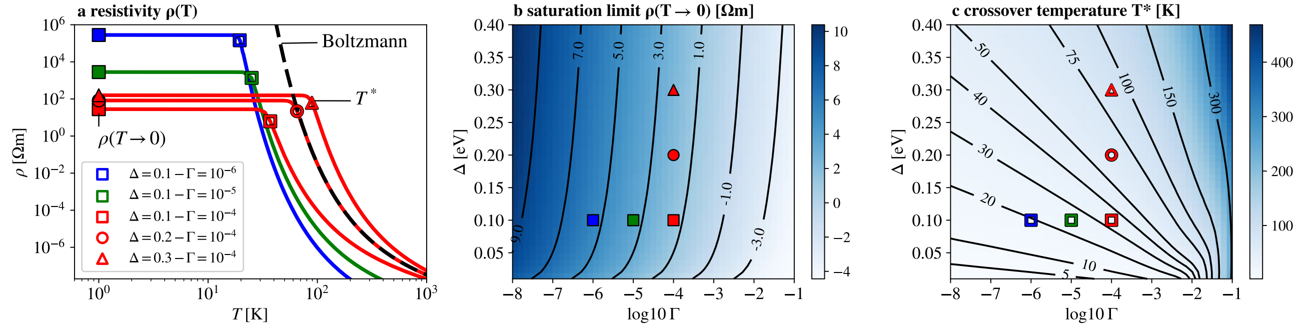

Fig. 4 Prototypical resistivity in correlated narrow-gap semiconductors. For a minimal two-band model, the figure shows: **a** The resistivity (lines) as a function of temperature for different gaps Δ and scattering rates Γ (both measured in eV). Closed symbols indicate the saturation limit $\rho(T\to 0)$; open symbols mark the inflection point $T^{\star}$—the lower (upper) bound of the semi-classical (quantum) regime. The semi-classical Boltzmann conductivity, Eq. (2), is shown as a dashed black line. **b** The saturation limit $\rho(T\to 0)$ (colored map; on a log-scale) as a function of Δ and Γ; black lines are iso-curves for indicated values; colored symbols mark the choices of Δ and Γ from **a**. **c** Crossover temperature $T^{\star}$ of the quantum regime. The data shows that $T^{\star}$ ($\rho(T\to 0)$) is dominantly controlled by Δ (Γ). Calculated for a three-dimensional half-filled two-band model with bare dispersions $\epsilon^0_{\mathbf{k}n} = (-1)^n[2t\sum_{i=1,3}\cos(k_i) + (6t+\Delta_0/2)]$ ($n=1,2$), with hopping $t = 0.25$ eV, a quasi-particle weight $Z = 1$, and a lattice constant $a = 1$ Å.

dominates transport. For this leading contribution to Eq. (1), we neglect band-dispersions and consider two levels (2L) $\epsilon_n = (-1)^n\Delta/2$ ($n = 1, 2$) separated by a gap Δ. Then, with $z = 1/2 + \beta/(2\pi)(\Gamma + i\Delta/2)$,

$$\sigma_{2\mathrm{L}}(T) \propto \frac{\beta}{\Gamma}\left[\mathrm{Re}\Psi'(z) - \frac{\beta\Gamma}{2\pi}\mathrm{Re}\Psi''(z)\right]. \tag{3}$$

This phenomenological quantum conductivity depends on two energy scales: Δ and Γ, and is very useful for analyzing experimental data, as shown below. A low-temperature expansion of Eq. (3) to second-order yields

$$\sigma_{2\mathrm{L}}(T) \propto \frac{\Gamma^2}{\left(\Delta^2+4\Gamma^2\right)^2}\left(1 + \frac{8\pi^2}{3}\frac{5\Delta^2-4\Gamma^2}{\left(\Delta^2+4\Gamma^2\right)^2}\left(k_{\mathrm{B}}T\right)^2\right) \tag{4}$$

resulting—for finite Γ—in the residual conductivity

$$\sigma_{2\mathrm{L}}(T=0) \propto \frac{\Gamma^2}{\left(\Delta^2+4\Gamma^2\right)^2}. \tag{5}$$

Unlike conduction by surface states in topological insulators, the quantum-regime conductivity depends on the bulk values Δ and Γ. Therefore, as a paramount distinction, residual conduction can be manipulated by pressure, while topological surface conduction is oblivious to it[22]. A direct consequence of Eq. (5) is the existence of a temperature T^* below which $\rho(T)$ must depart from Boltzmann behavior. Using Eq. (4), we can crudely estimate the dependencies of T^* via $\partial^2\rho(T)/\partial T^2 = 0$ (Supplementary Fig. S1):

$$k_{\mathrm{B}}T^* = \frac{1}{\sqrt{10}\pi}\left(\frac{\Delta}{2} + \frac{11}{5}\frac{\Gamma^2}{\Delta} + \mathcal{O}(\Gamma^4)\right) \tag{6}$$

For $\Gamma \ll \Delta$, T^* is essentially controlled by Δ—consistent with our numerical results and available experiments.

The take-away message is this: If Γ/Δ is not vanishingly small, the lifetime of intrinsic charge carriers manifests as a relevant energy scale. It introduces a coherence temperature T^*, delimits the applicability of Boltzmann theory from below, and leads to an algebraic saturation regime with residual conduction.

The quantum regime in experiments. Returning to $\mathrm{Ce_3Bi_4Pt_3}$, we anatomize the experimental conductivity vis-à-vis the characteristic temperature profile of the quantum regime established above. With the phenomenological conductivity, Eq. (3), we fit in Fig. 5 the data of (a) Cooley et al.[5] and (b) Wakeham et al.[6] and find near-perfect agreement: our Ansatz accurately reproduces the experimental temperature dependence for varying pressure and disorder.

We analyze trends in the fit parameters: as shown in the inset of Fig. 5a, we extract a gap Δ ~ 7.5meV at $P = 0$, which is largely enhanced for $P > 0$; also Γ increases with P. We extract smaller Γs and Δs for Wakeham et al.'s sample, see inset of Fig. 5b, owing to the overall smaller conductivity. Consistent with the degree of radiation damage, Γ increases with growing displacements per atom (DPA). The extracted Δ is congruent with activation-law fits above T^*[6] and increases only marginally under radiation. Note in Fig. 5a, for pressures $P > 4$GPa and very low temperatures, deviations from the quantum regime occur. There, as shown in ref. [5], $\sigma(T)$ matches 3D variable-range hopping (VRH) characteristics, $\propto \exp[(T/T_0)^{1/4}]$.

In Fig. 6, we perform a similar analysis for the bulk conductivity of the mixed-valence insulator $\mathrm{SmB_6}$[11], finding again excellent agreement. These results will be reviewed in the "Discussion" section.

Intermezzo: $\mathrm{Ce_3Bi_4Pt_3}$ at high pressures. Next, we briefly turn to $\mathrm{Ce_3Bi_4Pt_3}$ at high pressures, where Campbell et al.[7] found an insulator-to-metal crossover, cf. Fig. 3b. Indeed pressure-induced metallic phases are rather common for correlated semiconductors, e.g., for $\mathrm{SmB_6}$[23,24], CeRhSb[25], and FeSi[26]. We consider three candidate mechanisms: changes in (1) correlation effects, (2) the valence, (3) structural aspects. (1) Our many-body calculations reveal that pressure reduces electronic correlations: effective masses shrink from $m^*/m \sim 10$ at $P = 0$ (see also ref. [18]) to a mere ~2 at $P = 40$ GPa. Also, electron–electron scattering becomes less prevalent: the rate Γ is—for all pressures—of the form γT^2 (Fig. 2), with γ significantly decreasing with pressure. Reduced many-body renormalizations amplify the pressure enhancement of the non-interacting hybridization (see point (3), below), leading to larger gaps. In the absence of other factors, this is the canonical behavior of Kondo insulators. (2) Changes in the f-valency drive metal-insulator transitions, e.g., in rare-earth monochalcogenides[27]. In $\mathrm{Ce_3Bi_4Pt_3}$, congruent with experiment[5,7], pressure decreases (increases) the simulated 4f-occupation n_f (valence $4 - n_f$) from $n_f = 1.05$ ($P = 0$) to 0.96 ($P = 40$GPa)—while temperature has little influence[28]. $4f^0$ ($J = 0$) admixtures augment with P—accounting for the larger valence. Yet, also $4f^2$ (and $4f^1$ with $J = 7/2$) contributions grow—increasing the mixed-

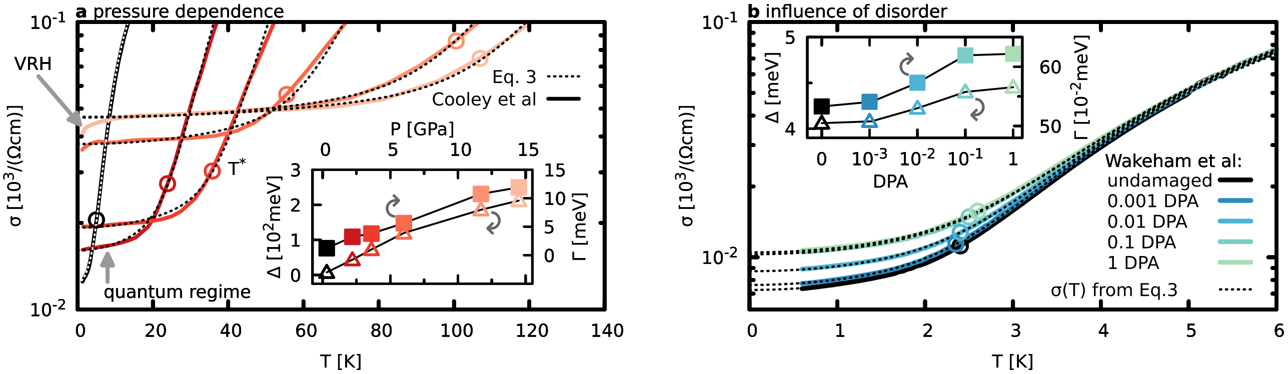

Fig. 5 Analysis of the quantum regime in $Ce_3Bi_4Pt_3$. We fit the conductivity $\sigma(T) = 1/\rho(T)$ from **a** Cooley et al.[5] (colored lines correspond to pressures indicated in the inset) and **b** Wakeham et al.[6] (colored lines indicate the degree of disorder quantified in displacements per atom (DPA)) with the phenomenological quantum conductivity Eq. (3) (dashed lines). The agreement is excellent: from a finite residual value for $T \to 0$, the conductivity grows algebraically (see the quantum regime formula: Eq. (4)) up to the crossover temperature T^* (circles). Above, higher powers in T become relevant as $\sigma(T)$ enters the exponential (semi-classical) regime. For pressures $P > 4$ GPa and very low T, the experimental conductivity deviates from the quantum regime and instead matches 3D variable-range hopping (VRH) characteristics, $\propto \exp[(T/T_0)^{1/4}]$[5]. The fit parameters Δ and Γ are given in the insets.

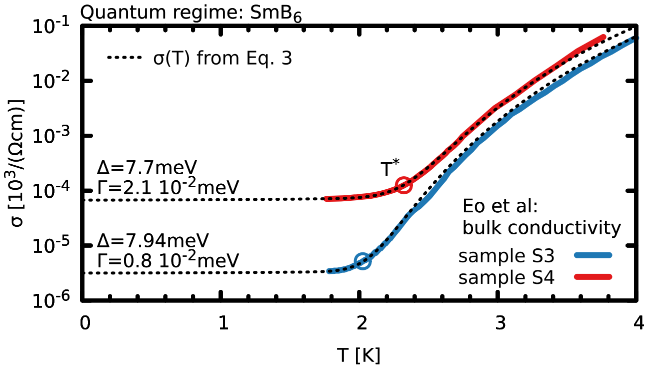

Fig. 6 Bulk conductivity of SmB_6. Low-T transport in SmB_6 is dominated by surface contributions[11,38–40]. With an inverted resistance setup, Eo et al.[11] eliminated the latter and extracted the bulk conductivity, reproduced here for two samples, in order of growing off-stoichiometry: S3, S4. Crucially, bulk conduction still saturates below T^* (inflection points in $\rho(T)$, circles). We fit the experiment using the phenomenological quantum conductivity Eq. (3). The excellent agreement suggests that the bulk resistivity in SmB_6 is lifetime-limited. Gaps Δ are fixed to indicated values obtained in ref. [11] from activation laws, $\exp(\Delta/(2k_BT))$, above 3 K. We extract a scattering rate Γ that increases by more than two-fold for an off-stoichiometry that almost doubles from S3 to S4[11]. For cleaner samples S1 and S2, experimental noise is large and T^* moves outside the measured temperature window, see Supplementary Fig. S3. From all samples combined, we extract: $T^* \propto \Gamma^{1/8}$.

valence character. Still, the probability of finding the system in a $4f^1$-state with $J = 5/2$ merely decreases quantitatively from 80% ($P = 0$) to ~55% ($P = 40$GPa)—excluding a dominantly valence-driven metallization. (3) Instead, we unravel the non-monotonic transport to originate from two counter-acting structural trends within the confines of spacegroup $I\bar{4}3d$: globally, pressure shrinks the lattice, enhancing hybridization gaps. While the atomic coordinates of Ce and Pt are dictated by symmetry, the local Bi position (u, u, u) may vary. Minimizing total energies, we find $u = 0.088$ at $P = 0$—in agreement with the experimental $u = 0.086$[29]—and predict a much larger $u = 0.097$ at $P = 40$GPa (Supplementary Fig. S2). This seemingly minute modification drastically changes inter-atomic hybridizations: instead of a monotonic increase (realized for $u = $ const), a critical pressure emerges above which the gap decreases. Hence, $Ce_3Bi_4Pt_3$ exhibits a peculiar high-pressure behavior, not canonical for Kondo insulators in general.

Discussion

The above results strongly suggest that electronic scattering is the microscopic driver of the resistivity saturation in $Ce_3Bi_4Pt_3$. Our mechanism is relevant also for other Kondo insulators. Indeed, iso-structural $Ce_3Sb_4Pt_3$ displays a $\rho(T)$[30] consistent with our understanding: different growth techniques (varying amounts of disorder) lead to largely different $\rho(T \to 0)$ while T^* changes little[30]. $Ce_3Bi_4Pd_3$, has recently been characterized as a semi-metal[31] or a Kondo insulator[32]. That the gap is next to non-existing[31,32] has been ascribed to spin–orbit[31] or Kondo[33] coupling effects. Here, we conjecture that under compression a resistivity plateau develops in $Ce_3Bi_4Pd_3$. Future transport and susceptibility measurements could then elucidate whether pressurized $Ce_3Bi_4Pd_3$ mimics $Ce_3Bi_4(Pd_{1-x}Pt_x)_3$ for small x—(dis) favouring the (spin–orbit) Kondo scenario. Saturation tendencies have also been found in the Kondo insulators $CeFe_2Al_{10}$[34] and pressurized $CeRu_4Sn_6$[35–37]. However, Kondo physics is not a prerequisite for our mechanism. What makes these systems natural hosts for the quantum regime are their small gaps $\Delta \sim \mathcal{O}(\lesssim 50$ meV). Correlation effects also drive narrow gaps in SmB_6[11,38–40], YbB_{12}[41], $U_3Sb_4Pt_3$[42], or $FeSb_2$[43], all of which exhibit saturation regimes, while rather belonging to the class of intermediate-valence insulators or d-electron intermetallics[4].

Yet, how can we ascertain that the presented microscopic scenario is at work in any such compound? Salient signatures of the quantum regime provide guidance: T^* correlates with the bulk gap and the residual conductivity increases with shrinking lifetimes. In $U_3Sb_4Pt_3$, the gap is unaffected by pressure, and—consistently—so is T^*[42]. In mixed-valence SmB_6, however, the activation gap shrinks under pressure, while T^* is hardly affected[23,24], and added disorder at first increases the resistivity[6]. Also in $CeRu_4Sn_6$ single crystals, pressure significantly increases activation energies, while T^* remains inert[37]. These observations are incompatible with our scenario and suggest a different origin to dominate residual conduction. Incidentally, for the latter two compounds conducting surface states of proposedly topological character[44,45] have been evidenced[6,11]. Note, however, that more disordered, polycrystalline samples of $CeRu_4Sn_6$ exhibit an additional inflection point in $\rho(T)$, which—consistent with our theory—moves up under compression[46]. Also for SmB_6, the situation is more complex: using a special measurement setup, Eo et al.[11] were able to disentangle surface and bulk contributions to conduction. Crucially, the isolated bulk conductivity still exhibits a saturation regime—whose temperature profile defies all previous scenarios[11,47]. As we demonstrate in Fig. 6, the phenomenological quantum conductivity Eq. (3) delivers an accurate description of the experimental data—providing strong evidence that the bulk resistivity in SmB_6 is lifetime-limited. Noteworthy, our theory shares its key ingredient with the scenario of Shen and Fu[48] that suggests finite lifetimes of Landau levels to account for quantum oscillations, e.g., in SmB_6[49,50].

In conclusion, we pinpoint finite lifetimes of intrinsic bulk carriers as a driver for residual conduction in semiconductors. Using a simple phenomenology, we demonstrated the characteristic temperature profile associated with this scenario to accurately match the saturation regimes in several materials. Possible microscopic sources for a finite scattering amplitude at low-T are impurities, other forms of disorder, and zero-point fluctuations. Indeed, the resistivity of no semiconductor in practice diverges for $T\rightarrow 0$. In the absence of other factors (or, see SmB_6, in combination with), signatures of the presented physics can therefore be expected to be ubiquitous in correlated narrow-gap semiconductors.

Methods

Realistic many-body electronic structure. We simulate $Ce_3Bi_4Pt_3$ at finite pressures using lattice constants from experimental fits to the third-order Birch–Murnaghan equation-of-state[7]. While the Wyckoff site 12a (12b) uniquely defines the placement of Ce (Pt) atoms, we relax the internal positions of Bi in density-functional theory (DFT) as implemented in WIEN2k[51] using the PBE functional. Band-structure results are summarized in Supplementary Fig. S2. Realistic dynamical mean-field theory (DFT+DMFT) calculations[52] are performed with the code of Haule et al.[53], including charge self-consistency, spin–orbit coupling, and using a continuous-time quantum Monte Carlo solver. Rotationally invariant interactions for the Ce-4f shell were parametrized by a Hubbard $U=5.5$eV and Hund's $J=0.68$eV (see also Supplementary Note 2) in conjunction with the nominal double-counting scheme[53]; Ce-4f hybridizations were allowed in an energy window of ±10 eV around the Fermi level. At ambient pressure, this setup yielded excellent results for spectral and optical properties[18] (see also ref. [54]). For illustrative purposes, we extract from the self-energy $\Sigma(\omega)$ a scattering rate Γ by averaging over the total angular momentum $J=5/2$ components that dominate spectral weight near the Fermi level: $\Gamma=-\left\langle \mathrm{Im}\Sigma(\omega=0)\right\rangle_{J=5/2}$. Finding that always $\Gamma(T)\propto T^2$, we quadratically extrapolate the minima in $\mathrm{Im}\Sigma(\omega)$ toward zero for temperatures beyond the reach of quantum Monte Carlo simulations, assuming that the frequency-dependence and the real-part do not change. Besides renormalizations from electronic correlations, we mimic the effect of disorder[20] with an additive, temperature-independent Γ_{imp}, typical for impurity scattering. In all cases, the crossover temperature T^* occurs in a regime in which scattering is largely dominated by Γ_{imp}. Since we are interested in the system's properties around and below T^*, uncertainties in the extrapolation of $\Gamma(T)$ are negligible.

Transport properties

Methodology. Resistivities for $Ce_3Bi_4Pt_3$ (Figs. 2 and 3) are simulated in linear-response theory using the full self-energy $\Sigma(\omega)$ as described in ref. [55]. High-precision transport calculations that evaluate Eq. (1) for a two-band model (Fig. 4) are performed using `LINRETRACE`[56]. The realistic conductivities require a sizable additional scattering rate Γ_{imp} (broadening) for numerical stability. Comparing the resistivities in Figs. 1 and 2, we see that simulated absolute values are on par with data from Katoh et al.[57]. Experiments with better residual-resistance ratios[5–7], have higher resistivities—suggesting that the broadening necessary in the simulations is too large for quantitatively mimicking high-quality samples. For simplicity, Γ_{imp} was only included in the transport simulations, not the DMFT. In Supplementary Fig. S4, we show that this leads to a small underestimation of $\mathrm{Im}\Sigma$ at low pressures. `LINRETRACE`[56], instead, yields numerically exact results for arbitrary scattering rates.

Expression of the conductivity. The derivation of the central Eq. (1) (outlined in Supplementary Note 1) uses contour integration techniques for the usual Kubo linear response for intra-band optical transitions with a static scattering rate[58], neglecting—in the DMFT spirit[52]—particle-hole couplings. This omission of vertex corrections is deliberate: we demonstrate that already the one-loop approximation possesses an intricate (and hitherto unknown) structure that qualitatively describes the resistivity saturation. We can motivate that, here, vertex corrections do not change the qualitative picture: impurity corrections to the current vertex of intrinsic carriers via ladder diagrams mainly reduce the decay rate Γ in the response function's prefactor by filtering out forward scattering[59], i.e., they do not change the essential physics. Corrections from crossed diagrams can be important, e.g., in doped semiconductors where they may lead to metal-to-insulator transitions via localization. Here, instead, we are concerned with metallic signatures in an a priori insulating host. Deviations from activated behavior could still be provided by extrinsic in-gap states: (a) through pinning of the chemical potential in an exhaustion regime, or in-gap states could themselves conduct, leading to (b) effectively smaller gap energies (gapped in-gap states), or (c) corrections from metallic but (weakly) localized in-gap states. Mechanisms (a,b) would lead to a resuming activated behavior at lower T, which is not observed in $Ce_3Bi_4Pt_3$. Route (c) as well as anti-localization effects would have characteristic signatures in the magnetoresistance, but are absent in $Ce_3Bi_4Pt_3$[7,60]. Further, Kondo-hole conduction[8,9], owing to Ce-off-stoichiometry, produces metallic slopes, $d\rho/dT>0$, not seen here. Our scenario thus provides a new interpretation to controversial in-gap states in Kondo insulators: we argue that they may derive from intrinsic valence and conduction states. The latter's finite (disorder-limited) lifetime causes incoherent weight to spill into the gap. For lifetime effects on quasi-particle transport in correlated metals, see, e.g., refs. [61,62].

Fermi velocities. Standard Peierls velocities in the band-basis only account for intra-band transitions (to incorporate inter-band transitions, see ref. [63]). For a discussion of intra- and inter-orbital transitions in the realistic simulations, that use full (intra+inter) dipolar transition elements, see Supplementary Fig. S5.

Data analysis. Crossover temperatures T^* are extracted from the simulations of $\rho(T)$ at discrete temperature points using derivatives of a cubic spline interpolation. Experimental curves are fitted with the approximative formula, Eq. (3), which neglects the momentum dependence of excitations. As illustrated in Supplementary Fig. S6, this assumption generally leads to an overestimation of, both, Δ and Γ. Bare scattering rates Γ_0 (in analogy to Γ_{imp} in Fig. 2), are obtained by multiplying Γ with the mass enhancement $m^*/m=1/Z$. Because m^*/m decreases with P (see text), the pressure-driven increase in Γ_0 is smaller than for Γ.

Data availability

The simulation data is available at https://doi.org/10.5281/zenodo.4355597 upon publication.

Code availability

A minimal python script `quantum_conductivity_fit.py` with which experimental conductivities or resistivities can be readily analyzed via Eq. (3) (Supplementary Fig. S7) is available at http://github.com/linretrace/quantum_conductivity_fit. The transport package `LINRETRACE` will become publicly available at http://github.com/linretrace/linretrace in 2021.

Received: 8 April 2021; Accepted: 8 September 2021;
Published online: 11 October 2021

References

1. Aeppli, G. & Fisk, Z. Kondo insulators. *Comments Cond. Mat. Phys* **16**, 150–170 (1992).
2. Riseborough, P. S. Heavy fermion semiconductors. *Adv. Phys.* **49**, 257–320 (2000).
3. Wirth, S. & Steglich, F. Exploring heavy fermions from macroscopic to microscopic length scales. *Nat. Rev. Mater.* **1**, 16051 EP (2016).
4. Tomczak, J. M. Thermoelectricity in correlated narrow-gap semiconductors. *J. Phys. Condens. Matter* **30**, 183001 (2018).
5. Cooley, J. C., Aronson, M. C. & Canfield, P. C. High pressures and the Kondo gap in $Ce_3Bi_4Pt_3$. *Phys. Rev. B* **55**, 7533–7538 (1997).
6. Wakeham, N. et al. Low-temperature conducting state in two candidate topological Kondo insulators: SmB_6 and $Ce_3Bi_4Pt_3$. *Phys. Rev. B* **94**, 035127 (2016).
7. Campbell, D. J. et al. Pressure-driven valence increase and metallization in the Kondo insulator $Ce_3Bi_4Pt_3$. *Phys. Rev. B* **100**, 235133 (2019).
8. Riseborough, P. S. Collapse of the coherence gap in Kondo semiconductors. *Phys. Rev. B* **68**, 235213 (2003).
9. Pietrus, T., Löhneysen, H. V. & Schlottmann, P. Kondo-hole conduction in the La-doped Kondo insulator $Ce_3Bi_4Pt_3$. *Phys. Rev. B* **77**, 115134 (2008).
10. Dzero, M., Sun, K., Galitski, V. & Coleman, P. Topological Kondo insulators. *Phys. Rev. Lett.* **104**, 106408 (2010).
11. Eo, Y. S. et al. Transport gap in SmB_6 protected against disorder. *Proc. Natl Acad. Sci. USA* **116**, 12638–12641 (2019).
12. Hundley, M. F., Canfield, P. C., Thompson, J. D., Fisk, Z. & Lawrence, J. M. Hybridization gap in $Ce_3Bi_4Pt_3$. *Phys. Rev. B* **42**, 6842–6845 (1990).
13. Takeda, Y. et al. Temperature-dependent high-resolution photoemission study of the Kondo insulator $Ce_3Bi_4Pt_3$. *J. Electron Spectrosc.* **101-103**, 721–724 (1999).
14. Bucher, B., Schlesinger, Z., Canfield, P. C. & Fisk, Z. Kondo coupling induced charge gap in $Ce_3Bi_4Pt_3$. *Phys. Rev. Lett.* **72**, 522–525 (1994).

15. Boebinger, G. S., Passner, A., Canfield, P. C. & Fisk, Z. Studies of the Kondo insulator $Ce_3Bi_4Pt_3$ in 61T pulsed magnetic fields. *Phys. B* **211**, 227–229 (1995).
16. Jaime, M. et al. Closing the spin gap in the Kondo insulator $Ce_3Bi_4Pt_3$ at high magnetic fields. *Nature* **405**, 160–163 (2000).
17. Doniach, S. The Kondo lattice and weak antiferromagnetism. *Physica B+C* **91**, 231–234 (1977).
18. Tomczak, J. M. Realistic many-body theory of Kondo insulators: renormalizations and fluctuations in $Ce_3Bi_4Pt_3$. Preprint at http://arxiv.org/abs/1904.01346 [cond-mat.str-el] (2019).
19. Chang, P.-Y., Erten, O. & Coleman, P. Möbius Kondo insulators. *Nat. Phys.* **13**, 794 EP (2017).
20. Sen, S., Vidhyadhiraja, N. S., Miranda, E., Dobrosavljević, V. & Ku, W. Fragility of the Kondo insulating gap against disorder: Relevance to recent puzzles in topological Kondo insulators. *Phys. Rev. Res.* **2**, 033370 (2020).
21. Poncé, S., Li, W., Reichardt, S. & Giustino, F. First-principles calculations of charge carrier mobility and conductivity in bulk semiconductors and two-dimensional materials. *Rep. Prog. Phys.* **83**, 036501 (2020).
22. Cai, S. et al. Independence of topological surface state and bulk conductance in three-dimensional topological insulators. *npj Quantum Mater.* **3**, 62 (2018).
23. Gabáni, S. et al. Pressure-induced Fermi-liquid behavior in the Kondo insulator SmB_6: possible transition through a quantum critical point. *Phys. Rev. B* **67**, 172406 (2003).
24. Zhou, Y. et al. Quantum phase transition and destruction of Kondo effect in pressurized SmB_6. *Sci. Bull.* **62**, 1439–1444 (2017).
25. Uwatoko, Y. et al. Pressure collapse of Kondo gap in Kondo compound CeRhSb. *J. Phys. Soc. Jpn* **65**, 27–29 (1996).
26. Hearne, G. R., Musyimi, P., Bhattacharjee, S., Forthaus, M. K. & Abd-Elmeguid, M. M. Unusual pressure-induced metallic state in the correlated narrow band-gap semiconductor FeSi. *Phys. Rev. B* **100**, 155118 (2019).
27. Jarrige, I. et al. Unified understanding of the valence transition in the rare-earth monochalcogenides under pressure. *Phys. Rev. B* **87**, 115107 (2013).
28. Kwei, G. H., Lawrence, J. M. & Canfield, P. C. Temperature dependence of the 4f occupation of $Ce_3Bi_4Pt_3$. *Phys. Rev. B* **49**, 14708–14710 (1994).
29. Kwei, G. H. et al. Thermal expansion of $Ce_3Bi_4Pt_3$ at ambient and high pressures. *Phys. Rev. B* **46**, 8067–8072 (1992).
30. Jones, C. D. W., Regan, K. A. & DiSalvo, F. J. Thermoelectric properties of the doped Kondo insulator: $Nd_xCe_{3-x}Pt_3Sb_4$. *Phys. Rev. B* **58**, 16057–16063 (1998).
31. Dzsaber, S. et al. Kondo insulator to semimetal transformation tuned by spin-orbit coupling. *Phys. Rev. Lett.* **118**, 246601 (2017).
32. Kushwaha, S. K. et al. Magnetic field-tuned Fermi liquid in a Kondo insulator. *Nat. Commun.* **10**, 5487 (2019).
33. Tomczak, J. M. Isoelectronic tuning of heavy fermion systems: Proposal to synthesize $Ce_3Sb_4Pd_3$. *Phys. Rev. B* **101**, 035116 (2020).
34. Muro, Y., Yutani, K., Kajino, J., Onimaru, T. & Takabatake, T. Anisotropic c–f hybridization in the Kondo semiconductor $CeFe_2Al_{10}$. *J. Korean Phys. Soc.* **63**, 508–511 (2013).
35. Das, I. & Sampathkumaran, E. V. Electrical-resistance anomalies in a Ce-Ru-Sn phase. *Phys. Rev. B* **46**, 4250–4252 (1992).
36. Strydom, A. M., Guo, Z., Paschen, S., Viennois, R. & Steglich, F. Electronic properties of semiconducting $CeRu_4Sn_6$. *Phys. B Condens. Matter* **359–361**, 293–295 (2005).
37. Zhang, J. et al. Pressure effect in the Kondo semimetal $CeRu_4Sn_6$ with nontrivial topology. *Chin. Phys. B* **27**, 097103 (2018).
38. Wolgast, S. et al. Low-temperature surface conduction in the Kondo insulator SmB_6. *Phys. Rev. B* **88**, 180405 (2013).
39. Kim, D. J. et al. Surface Hall effect and nonlocal transport in SmB_6: evidence for surface conduction. *Sci. Rep.* **3**, 3150 (2013).
40. Syers, P., Kim, D., Fuhrer, M. S. & Paglione, J. Tuning bulk and surface conduction in the proposed topological Kondo insulator SmB_6. *Phys. Rev. Lett.* **114**, 096601 (2015).
41. Sato, Y. et al. Unconventional thermal metallic state of charge-neutral fermions in an insulator. *Nat. Phys.* **15**, 954–959 (2019).
42. Canfield, P. C. et al. Doping and pressure study of $U_3Sb_4Pt_3$. *J. Alloys Compd.* **181**, 77–81 (1992).
43. Sun, P. et al. Highly dispersive electron relaxation and colossal thermoelectricity in the correlated semiconductor $FeSb_2$. *Phys. Rev. B* **88**, 245203 (2013).
44. Xu, Y., Yue, C., Weng, H. & Dai, X. Heavy Weyl fermion state in $CeRu_4Sn_6$. *Phys. Rev. X* **7**, 011027 (2017).
45. Thunström, P. & Held, K. Topology of SmB_6 determined by dynamical mean field theory. *Phys. Rev. B* **104**, 075131 (2021).
46. Sengupta, K., Iyer, K. K., Ranganathan, R. & Sampathkumaran, E. V. Unusual pressure response of electronic transport properties of a Kondo insulator $CeRu_4Sn_6$. *J. Phys.* **377**, 012029 (2012).
47. Harrison, N. Highly asymmetric nodal semimetal in bulk SmB_6. *Phys. Rev. Lett.* **121**, 026602 (2018).
48. Shen, H. & Fu, L. Quantum oscillation from in-gap states and a non-hermitian landau level problem. *Phys. Rev. Lett.* **121**, 026403 (2018).
49. Li, G. et al. Two-dimensional Fermi surfaces in Kondo insulator SmB_6. *Science* **346**, 1208–1212 (2014).
50. Tan, B. S. et al. Unconventional Fermi surface in an insulating state. *Science* **349**, 287–290 (2015).
51. Blaha, P. et al. Wien2k: An APW+lo program for calculating the properties of solids. *J. Chem. Phys.* **152**, 074101 (2020).
52. Georges, A., Kotliar, G., Krauth, W. & Rozenberg, M. J. Dynamical mean-field theory of strongly correlated fermion systems and the limit of infinite dimensions. *Rev. Mod. Phys.* **68**, 13 (1996).
53. Haule, K., Yee, C.-H. & Kim, K. Dynamical mean-field theory within the full-potential methods: Electronic structure of $CeIrIn_5$, $CeCoIn_5$, and $CeRhIn_5$. *Phys. Rev. B* **81**, 195107 (2010).
54. Cao, C., Zhi, G.-X. & Zhu, J.-X. From trivial Kondo insulator $Ce_3Pt_3Bi_4$ to topological nodal-line semimetal $Ce_3Pd_3Bi_4$. *Phys. Rev. Lett.* **124**, 166403 (2020).
55. Tomczak, J. M., Haule, K. & Kotliar, G. Signatures of electronic correlations in iron silicide. *Proc. Natl. Acad. Sci. USA* **109**, 3243–3246 (2012).
56. Pickem, M., Maggio, E. & Tomczak, J. M. LinReTraCe: The Linear Response Transport Centre. http://github.com/linretrace (2021).
57. Katoh, K. & Takabatake, T. Crystal growth and semiconducting properties of Ce_3 Bi_4 Pt_3. *J. Alloys Compd.* **268**, 22–24 (1998).
58. Tomczak, J. M., Haule, K., Miyake, T., Georges, A. & Kotliar, G. Thermopower of correlated semiconductors: Application to $FeAs_2$ and $FeSb_2$. *Phys. Rev. B* **82**, 085104 (2010).
59. Coleman, P. *Introduction to Many-Body Physics* (Cambridge University Press, 2015).
60. Hundley, M. F., Lacerda, A., Canfield, P. C., Thompson, J. D. & Fisk, Z. Magnetoresistance of the Kondo insulator $Ce_3Bi_4Pt_3$. *Phys. B* **186-188**, 425–427 (1993).
61. Deng, X. et al. How bad metals turn good: Spectroscopic signatures of resilient quasiparticles. *Phys. Rev. Lett.* **110**, 086401 (2013).
62. Xu, W., Haule, K. & Kotliar, G. Hidden Fermi liquid, scattering rate saturation, and Nernst effect: a dynamical mean-field theory perspective. *Phys. Rev. Lett.* **111**, 036401 (2013).
63. Tomczak, J. M. & Biermann, S. Optical properties of correlated materials: generalized Peierls approach and its application to VO_2. *Phys. Rev. B* **80**, 085117 (2009).

Acknowledgements

We acknowledge discussions with D.J. Campbell and J. Paglione and thank them for sharing unpublished information on atomic positions from their pressure experiments. We are grateful to F. Ronning, N. Wakeham, and J.D. Thompson for providing experimental raw data from ref. [6]. This work has been supported by the Austrian Science Fund (FWF) through project `LINRETRACE` P 30213-N36. Calculations were partially performed on the Vienna Scientific Cluster (VSC).

Author contributions

J.M.T. conceived the project. M.P. and E.M. developed and implemented the `LINRETRACE` methodology, performed transport simulations, and analyzed the data. J.M.T. performed many-body simulations and wrote the manuscript with input from all authors.

Competing interests

The authors declare no competing interests.

Additional information

Supplementary information The online version contains supplementary material available at https://doi.org/10.1038/s42005-021-00723-z.

Correspondence and requests for materials should be addressed to Jan M. Tomczak.

Peer review information *Communications Physics* thanks Chao Cao, Jernei Mravlje and the other, anonymous, reviewer(s) for their contribution to the peer review of this work. Peer reviewer reports are available.

Reprints and permission information is available at http://www.nature.com/reprints

Publisher's note Springer Nature remains neutral with regard to jurisdictional claims in published maps and institutional affiliations.

Open Access This article is licensed under a Creative Commons Attribution 4.0 International License, which permits use, sharing, adaptation, distribution and reproduction in any medium or format, as long as you give appropriate credit to the original author(s) and the source, provide a link to the Creative Commons license, and indicate if changes were made. The images or other third party material in this article are included in the article's Creative Commons license, unless indicated otherwise in a credit line to the material. If material is not included in the article's Creative Commons license and your intended use is not permitted by statutory regulation or exceeds the permitted use, you will need to obtain permission directly from the copyright holder. To view a copy of this license, visit http://creativecommons.org/licenses/by/4.0/.

© The Author(s) 2021